Enhanced plateau effect at resonance in realistic nonintegrable extreme-mass-ratio inspirals

Areti Eleni[*] and Theocharis A. Apostolatos[†]

Section of Astrophysics, Astronomy, and Mechanics, Department of Physics, University of Athens, Panepistimiopolis Zografos GR15783, Athens, Greece

(Received 2 July 2023; accepted 12 September 2023; published 18 December 2023)

When an extreme-mass-ratio inspiral involving a nonintegrable gravitational field, such as a deformed Kerr black hole, undergoes a prolonged resonance, the frequencies that engage in resonance retain a fixed rational ratio, despite experiencing gradual changes due to radiation reaction. In the past this plateau effect in the evolution of the ratio of frequencies has been investigated by studying the orbital evolution through kludge models, which provide approximate average losses of energy and angular momentum experienced by a test particle in this field. By employing a Newtonian gravitational field that closely resembles a pure Kerr or a perturbed Kerr relativistic field, we demonstrate that the actual evolution of an orbit driven by artificial "self-force" results in more prolonged periods of resonance crossings compared to those obtained by imposing a predetermined rate of energy and angular momentum change throughout the orbital progression.

DOI: 10.1103/PhysRevD.108.124044

I. INTRODUCTION

Extreme-mass-ratio inpirals (EMRIs), are prominent sources of gravitational waves (GWs) for the future space-based detector Laser Interferometer Space Antenna (LISA) [1]. EMRIs are binaries consisting of a stellar mass compact object, i.e., a black hole (BH) or a neutron star (NS) of mass m, inspiraling around a supermassive BH of mass M, with mass ratio $\epsilon = m/M \leq 10^{-4}$.

Since the lighter compact object of an EMRI spends the last few years of its inspiral tracing out the strong-gravity region of the supermassive BH, EMRIs offer us the opportunity to test the theory of general relativity (GR) and its astrophysical implications concerning the formation of black holes. The last hundreds of thousands of GW cycles of such a system encode the details of the spacetime geometry of the massive object; thus by analyzing these waves, one could read out its multipole moments [2].

According to GR the gravitational field of an astrophysical BH is described by the Kerr metric [3], the multipole moments of which are determined only by its mass and spin [4,5]. Since the Kerr metric is characterized by a few symmetries, the equations governing the geodesic motion around a Kerr BH form an integrable system. The conservation of the energy and z-angular momentum along the axis of symmetry is associated with a time-translation and a rotational Killing vector, respectively, while the existence of the Carter constant [6] is linked to a hidden symmetry of a rank-2 Killing tensor. As a consequence, a bound geodesic Kerr orbit in the spatial part of the phase-space is confined to lie on a compact torus characterized by three fundamental frequencies [7]. Trajectories ergodically fill the phase-space tori, unless two or more fundamental frequencies form a rational ratio (resonant orbits).

However, the actual orbit of the small compact object around the massive BH is not exactly geodesic, due to the gravitational self-force (SF) which arises from the object's interaction with the time-dependent gravitational field [8,9]. The dissipative part of SF drives the object to a gradual inspiral towards the massive BH, following an adiabatic evolution of geodesics, while it radiates away energy and angular momentum in the form of GWs. The orbital motion is obtained from BH perturbation theory with the small mass ratio ϵ as an expansion parameter [10,11]. The SF for a nonspinning particle on a generic orbit around a Kerr BH to first order in the mass ratio ϵ has been obtained recently [12].

During the inspiral the three orbital fundamental frequencies change slowly, thus a resonance will occur when two of them form a rational ratio. The methods we normally use for computing the orbital evolution, and the corresponding waveforms, become inadequate at resonance, where the "constants" of motion then change rapidly, leading to large shifts in waveform's phase [13].

An important characteristic of resonances is that they can be used to discern if the background spacetime is not an integrable Kerr one, either because the central BH is not described by GR or due to the fact that the environment of the BH is not vacuum. Such spacetimes probably do not

[*]aeleni@phys.uoa.gr
[†]thapostol@phys.uoa.gr

possess all the special symmetries of Kerr that lead to a third integral of motion and form a complete integrable system. These cases could be described as appropriate deformations of Kerr metric. However, when an integrable Hamiltonian is slightly perturbed, its phase-space tori undergo changes. The Poincaré-Birkhoff theorem [14,15] states that the resonant tori disintegrate and form islands of stability (Birkhoff islands), occupying a phase-space volume of nonzero measure, inside which the ratio of frequencies remain locked to a constant rational value. Birkhoff islands are characteristic features of nonintegrable dynamical systems.

Reference [16] investigated the evolution of the ratio of the orbital frequencies of a particle orbiting around a non-Kerr object describing by the Manko-Novikov (MN) metric [17], when its trajectory crosses a Birkhoff island. Due to the lack of an expression for the radiation reaction SF for non-Kerr spacetimes, the numerical integration of an orbit was performed by combining the equations of geodesic motion for MN metric with the hybrid approximative method [18] which provides the average losses of energy and z-angular momentum. Assuming constant rates of energy and z-angular momentum losses, the time interval within which the orbit remains at a prolonged resonance (i.e., stays in a Birkhoff island) was computed. During that time both frequencies change while their ratio remains constant. Whenever such a plateau in the evolution of the ratio of frequencies is observed one could conclude that the central object is not a Kerr BH. Also, in [19], following a similar procedure, Destounis *et al.* found that when the orbit crosses a prolonged resonance, a rapid but short-lived "glitch" shows up in gravitational waveforms.

In the present work we would like to address the question whether the assumption of constant rates of change of energy and z-angular momentum leads to wrong estimates of the time interval of resonance crossings. Lacking a SF formula for a non-Kerr spacetime, we will resort to a Newtonian analog problem.

In Ref. [20] it was shown that the Euler gravitational field of a pair of spatially fixed point masses at an imaginary distance from each other, is a very good analog of the Kerr relativistic field. Moreover, this particular field can be modified so as to transform the system from an integrable to a slightly nonintegrable one. By incorporating an additional small external dissipative force, we could drive adiabatically an orbit, in a similar fashion that a geodesic orbit is driven in a given background spacetime by the radiation reaction caused by a self-force. At the same time, the average losses of energy and z-angular momentum in the adiabatic limit for such a dissipative force are computed. Once again, the orbit is evolved by a new integration scheme, based on inducing the subsequent time-depending "constants" of motion, but without any direct dissipative force implied. Finally the two distinctive numerical schemes were compared with respect to the total resonance crossing time. There was a systematic enhancement of the crossing time, by a factor of at least 2, when the instantaneous dissipative force was employed.

The rest of the article is organized as follows: In Sec. II an overall description of the oblate Euler problem is given. In Sec. III we describe the perturbed version of this problem, constructed by introducing a small mass at the midpoint between the two fixed masses. In Sec. IV we give a brief description of some theoretical features of slightly nonintegrable problems. In Sec. V, we introduce the dissipative force that is used in this paper and explain the two different integration schemes followed to drive an orbit in the perturbed Euler field. The scheme based on average losses is further analyzed in Sec. VI. Finally, in Sec. VII we present our results and discuss their implications.

II. THE OBLATE EULER PROBLEM

The Euler problem of two fixed centers [21] describes the gravitational field of two static point masses m_1 and m_2 at a fixed distance $2a$ between them. We assume that the z-axis is the axis along which the two masses are located at $z_1 = a\hat{z}$ and $z_2 = -a\hat{z}$, respectively, with a being constant and real. By setting the two masses equal to each other, i.e., $m_1 = m_2 = M/2$, and their distance imaginary, i.e., $a \to ia$, the potential becomes oblate (with negative quadrupole moment) and can be considered as the Newtonian analog of the relativistic Kerr black hole [3,20,22–24]. We need the symmetric case with equal masses because only then the gravitational potential of each mass is complex conjugate to the potential of the other mass, allowing the combined potential field of the two masses to be real. The resulting gravitational field of the oblate Euler (also known as the Vinti potential in astronomy, used to describe the gravitational field around oblate planets [25]), is stationary, axisymmetric along the z-axis, and reflection symmetric about the equatorial plane. It is described by the following form:

$$V_0 = -\frac{G(M/2)}{|\mathbf{r} - ia\hat{\mathbf{z}}|} - \frac{G(M/2)}{|\mathbf{r} + ia\hat{\mathbf{z}}|}, \tag{1}$$

where $\mathbf{r}$ is the radial distance from the axes origin and by $|\mathbf{k}|$ we mean $\sqrt{\mathbf{k}\cdot\mathbf{k}}$. The latter vector product is a complex number and in order to keep the square root single valued we should adopt a branch cut. We have chosen the negative real axis of the vector product as the branch cut of our potential function so that the two denominators in (1) will be conjugate to each other leading to a real potential. Henceforth, when we mention the Euler field, we shall exclusively refer to the oblate Euler field, and later on to its perturbed version.

A general stationary, axisymmetric and reflection symmetric about the equatorial plane Newtonian potential that vanishes at infinity can be fully decomposed in multipole moments M_l through the relation [24,26],

$$V = -\sum_{l=0}^{\infty} \frac{M_{2l}}{r^{2l+1}} P_{2l}(z/r),$$

where P_l are the Legendre polynomials. It turns out that the multipole moments of the Euler potential (1) are given by [20,26],

$$M_{2l} = M(-a^2)^l,$$

which is the same as the "no-hair" relation obeyed by the mass multipole moments of the Kerr metric [4,5] with the length parameter a of the Euler field, playing the role of the spin of a Kerr black hole [20,24].

A more appropriate coordinate system to study the motion in this field is that of oblate spheroidal coordinates, (ξ, η, ϕ), where ϕ is the usual spherical azimuthal angle, $\xi \in [0, +\infty)$ and $\eta \in [-1, 1]$. These new coordinates are related to the Cartesian coordinates (x, y, z) by

$$x = a\sqrt{(1+\xi^2)(1-\eta^2)}\cos\phi,$$
$$y = a\sqrt{(1+\xi^2)(1-\eta^2)}\sin\phi,$$
$$z = a\xi\eta,$$

and to the spherical coordinates (r, θ) by

$$r = a\sqrt{1+\xi^2-\eta^2},$$
$$\cos\theta = \frac{\xi\eta}{\sqrt{1+\xi^2-\eta^2}}.$$

In terms of oblate spheroidal coordinates the Euler potential (1) assumes the following simple form:

$$V_0(\xi, \eta) = -\frac{GM_0\xi}{a(\xi^2+\eta^2)}. \tag{2}$$

From the above multipole expansion, $M_0 = M$. It should be noted that the field $V_0(\xi, \eta)$ is defined everywhere except when $\xi = 0$ and $\eta = 0$, which corresponds to the equatorial focal circle $(r = a, \theta = \pi/2)$, where the potential becomes singular. This singularity corresponds to Kerr's ring singularity.

The motion of a test particle in the Newtonian Euler potential is independent of its mass, so the Hamiltonian (per unit test-particle mass μ) is

$$H_0 = \frac{1}{2a^2}\left[p_\xi^2\frac{\xi^2+1}{\xi^2+\eta^2} + p_\eta^2\frac{1-\eta^2}{\xi^2+\eta^2} + \frac{p_\phi^2}{(\xi^2+1)(1-\eta^2)}\right] + V_0(\xi, \eta), \tag{3}$$

while the conjugate momenta to ξ, η, ϕ are defined as

$$p_\xi = a^2\frac{\xi^2+\eta^2}{\xi^2+1}\dot{\xi}, \tag{4}$$

$$p_\eta = a^2\frac{\xi^2+\eta^2}{1-\eta^2}\dot{\eta}, \tag{5}$$

$$p_\phi = a^2(\xi^2+1)(1-\eta^2)\dot{\phi}, \tag{6}$$

where "$\dot{}$" denotes time derivative. (The kinetic part of the Hamiltonian (3) is the usual Newtonian $(p_x^2 + p_y^2 + p_z^2)/2$ term in Cartesian coordinates, but translated in oblate spheroidal coordinates; see Ref. [27]).

The stationarity and axisymmetry of the system is obvious in the Hamiltonian expression H_0. The time and azimuthal coordinate are cyclic, leading to conservation of the energy $E = H_0$ and the angular momentum along the axis of symmetry $L_z = p_\phi$, respectively. Furthermore, the Hamilton-Jacobi equation is separable in oblate spheroidal coordinates, leading to a third nontrivial constant of motion, β, which is quadratic in momenta (see the classical book of Landau [27]). By substituting β by $-Q - L_z^2 - 2a^2E$, the quantity Q can be considered as the Newtonian analog of Kerr's Carter constant [6] obtaining either one of the following forms [20]:

$$Q = (1-\eta^2)p_\eta^2 + \eta^2\left(-2Ea^2 + \frac{L_z^2}{1-\eta^2}\right) \tag{7}$$

$$= -p_\xi^2(\xi^2+1) + 2a^2E\xi^2 + 2GMa\xi - \frac{L_z^2\xi^2}{\xi^2+1}. \tag{8}$$

The existence of a third integral of motion renders the Euler problem completely integrable in terms of quadratures; as there are three independent and in involution (i.e., $\{H_0, L_z\} = \{H_0, Q\} = \{L_z, Q\} = 0$) integrals of motion, as the number of the degrees of freedom of the corresponding Hamiltonian system. Equations (7) and (8) are quite similar to the corresponding expressions relating the Carter constant in Kerr with either p_θ and θ, or p_r and r.

An extensive list of key similarities that the Euler potential shares with the gravitational field of the relativistic Kerr black hole can be found in Ref. [20]. The analogy between the two problems is better revealed by replacing $a\xi$ and η of the Euler field with r and $\cos\theta$, respectively, mimicking the Boyer-Lindquist coordinates of Kerr. Actually, the equations of motion in a Kerr metric at the first post-Newtonian order and at large r-values reduce to the equations of motion in the Euler field [28]. On the other hand the Euler problem, being Newtonian, has no analog of an event horizon, like Kerr, so there are no orbits that are led to plunge behind a horizon; however we are only interested in orbits that simply lie in the strong field region.

III. THE PERTURBED EULER

We perturb the Euler field in order to find a Newtonian analog of a slightly perturbed Kerr spacetime, by adding a small point mass m ($m \ll M$) at the origin of the axes. In this case the expression of the quadrupole moment and all higher mass moments are different from those of the unperturbed Euler, now obeying the following relation:

$$M_0 = M + m, \tag{9}$$

$$M_{2l} = (-a^2)^l M, \tag{10}$$

with $l = 1, 2\ldots$. The multipole moments M_k with odd k vanish due to the reflection symmetry about the equatorial plane. The new potential in oblate spheroidal coordinates takes the form,

$$V(\xi,\eta) = -\frac{GM\xi}{a(\xi^2+\eta^2)} - \frac{Gm}{a\sqrt{1+\xi^2-\eta^2}}. \tag{11}$$

We will rewrite the potential in such a way that the unperturbed and the perturbed fields correspond to the same total mass M_0, so that both fields will be comparable with respect to their asymptotic behavior at infinity,

$$V(\xi,\eta) = -\frac{GM_0\xi}{a(\xi^2+\eta^2)} + \frac{Gm}{a}\left(\frac{\xi}{\xi^2+\eta^2} - \frac{1}{\sqrt{1+\xi^2-\eta^2}}\right). \tag{12}$$

When $m = 0$ the system degenerates into the integrable Euler problem. In all our numerical computations we assume $M_0 = 1$ and geometrized units. This fixes the timescale of our integrations.

When an integrable Hamiltonian system becomes slightly perturbed, the new Hamiltonian can be written in terms of the old integrable Hamiltonian H_0 plus a perturbation term H_1,

$$H = H_0 + \epsilon H_1. \tag{13}$$

In our case H_0 is the Hamiltonian given exactly by Eq. (3). We assume that the mass m is sufficiently small, compared to M_0, to apply classical perturbation theory. The term H_1 is given by

$$H_1 = \frac{GM_0}{a}\left(\frac{\xi}{\xi^2+\eta^2} - \frac{1}{\sqrt{1+\xi^2-\eta^2}}\right), \tag{14}$$

while the perturbative parameter is defined as $\epsilon = m/M_0$.

The new Hamiltonian has no dependence either on the time variable t or the azimuthal angle ϕ, due to the stationarity and axisymmetry of the new potential. As a result, there are still two constants of motion; the energy,

$$E = H = \frac{a^2}{2}(\xi^2+\eta^2)\left[\frac{\dot{\xi}^2}{1+\xi^2} + \frac{\dot{\eta}^2}{1-\eta^2}\right] + \frac{a^2}{2}(1+\xi^2)(1-\eta^2)\dot{\phi}^2 + V(\xi,\eta), \tag{15}$$

and the component of angular momentum along the axis of symmetry,

$$L_z = p_\phi = a^2(\xi^2+1)(1-\eta^2)\dot{\phi}. \tag{16}$$

However, the Hamilton-Jacobi equation is not separable anymore; there is no third integral of motion, which is independent and in involution with the energy, E, and the z-angular momentum, L_z. In the next sections we will numerically confirm the nonintegrability of the perturbed Euler, by investigating the Poincaré maps of orbits in the potential (12). Furthermore we will reveal properties related to nonintegrability, such as chaotic motion and Birkhoff chains, when $m \neq 0$.

As long as we are interested in bound orbits, we could define an effective potential $V_{\rm eff}$ to rewrite (15) as

$$0 = \frac{1}{2}a^2(\xi^2+\eta^2)\left(\frac{\dot{\xi}^2}{\xi^2+1} + \frac{\dot{\eta}^2}{1-\eta^2}\right) + V_{\rm eff}(\xi,\eta), \tag{17}$$

with

$$V_{\rm eff}(\xi,\eta) = \frac{L_z^2}{2a^2(\xi^2+1)(1-\eta^2)} + V(\xi,\eta) - E, \tag{18}$$

where (16) has been used to replace the centrifugal part of the kinetic energy. From Eq. (17), it is obvious that the motion is allowed only for $V_{\rm eff} \leq 0$. When an orbit reaches the curve $V_{\rm eff} = 0$, the velocities $\dot{\xi}$ and $\dot{\eta}$ both become zero (turning points); thus the curve $V_{\rm eff} = 0$ is known as the curve of zero velocity (CZV) [16]. Bound orbits are allowed in the interior of a closed CZV where the effective potential is negative. Additionally bound orbits are characterized by $E < 0$, since orbits with $E \geq 0$ have CZVs that are not closed but are extended to infinity. The number and the size of the distinct allowed regions on the poloidal plane (ξ,η), within which a bound orbit could evolve, depend on the values of E and L_z of the orbit itself.

On the equatorial plane, i.e., at $\eta = 0$, the effective potential reads,

$$V_{\rm eff,eq} = -E + \frac{L_z^2}{2a^2(\xi^2+1)} - \frac{GM_0}{a\xi}\left[1 - \epsilon\left(1 - \frac{\xi}{\sqrt{1+\xi^2}}\right)\right]. \tag{19}$$

Especially a circular equatorial orbit (CEO) at $\xi = \xi_0$ satisfies,

$$V_{\mathrm{eff,eq}}(\xi_0) = \left.\frac{\partial V_{\mathrm{eff,eq}}}{\partial \xi}\right|_{\xi_0} = 0. \tag{20}$$

Solving the system of the last two equations we obtain the constants of motion for a CEO,

$$L_z = \pm \frac{GM_0(\xi_0^2+1)}{\xi_0^{5/2}}\left[1-\epsilon\left(1-\frac{\xi_0^3}{(1+\xi_0^2)^{3/2}}\right)\right], \tag{21}$$

$$E = -\frac{GM_0}{2a\xi_0^3}(\xi_0^2-1)\left[1-\epsilon\left(1-\frac{\xi_0^3}{(\xi_0^2-1)\sqrt{1+\xi_0^2}}\right)\right]. \tag{22}$$

For stable circular equatorial orbits we should have $\frac{\partial^2 V_{\mathrm{eff,eq}}}{\partial \xi^2}\big|_{\xi_0} \geq 0$. An innermost stable circular orbit (ISCO) exists when $\frac{\partial^2 V_{\mathrm{eff,eq}}}{\partial \xi^2}\big|_{\xi_{\mathrm{ISCO}}} = 0$. The perturbed Euler, as well as the corresponding unperturbed one, has an ISCO with the corresponding value of ξ_{ISCO} depending only on the perturbative parameter ϵ. For $\epsilon = 0$, $\xi_{\mathrm{ISCO}} = \sqrt{3}$, see Ref. [20].

IV. KOLMOGOROV-ARNOLD-MOSER TORI AND RESONANT TORI

Due to the integrability of the Euler problem, bound orbits lie on a 2-dimensional toroidal surface in the 4-dimensional phase space $(\xi, \dot{\xi}, \eta, \dot{\eta})$, characterized by the three integrals of motion. Tori corresponding to orbits that are characterized by the same E and L_z but different Q are nested within each other. Using action-angle variables one can define the orbit's characteristic frequencies [20] of libration type $(\Omega_\xi, \Omega_\eta)$ associated with ξ and η oscillations. If the ratio of frequencies Ω_ξ/Ω_η is an irrational number, the motion will never repeat itself and it will gradually cover the whole torus (quasiperiodic orbit). When the ratio of frequencies is a rational number (resonance), instead, the orbit repeats itself after an integer number of windings on the corresponding resonant torus (periodic orbit).

The Poincaré surface of section is a two-dimensional surface that intersects transversely the foliage of tori [29]. In our case, we have chosen as a surface of section the plane $(\xi, \dot{\xi})$, when the orbit pierces the equatorial plane, $\eta = 0$, with positive $\dot{\eta}$. The Poincaré surface of section of each torus forms an invariant closed curve, which is either covered densely when the orbit is quasiperiodic, or consisting of finite fixed points when the orbit is periodic.

When an integrable Hamiltonian system becomes slightly perturbed, the Kolmogorov-Arnold-Moser (KAM) theorem [30–32] states that almost all tori (the nonresonant ones) become slightly deformed. Thus the quasiperiodic orbits survive under a sufficiently small perturbation. They are confined on a 2-torus (KAM torus) which is slightly deviating from the unperturbed one. Consequently the corresponding surface of section resembles the surface of section of the initially integrable system, but with a slightly deformed shape; these are the invariant KAM curves of the perturbed system.

The resonant tori, instead, are destroyed, when the system is slightly perturbed, according to the Poincaré-Birkhoff theorem [14,15], forming Birkhoff chains of islands on the Poincaré section. These islands are built around the fixed points of the initial unperturbed (integrable) system. The interior of these islands consists of a new family of KAM curves, all sharing the same rational ratio of fundamental frequencies as the corresponding resonant torus of the unperturbed system.

The Birkhoff islands of stability are very thin and their detection on a Poincaré section could become quite tedious. A useful method to study nonintegrable systems and numerically detect the location of a chain of islands is the so-called rotation number, which actually gives the ratio of the fundamental frequencies [33]. The rotation number ν_θ is defined by

$$\nu_\theta = \lim_{N\to\infty} \frac{1}{2\pi N}\sum_{i=1}^{N} \theta_i, \tag{23}$$

with N denoting the number of crossings of the Poincaré section by a phase-space trajectory. The angles of rotation θ_i are calculated as follows: at first one finds on the surface of section the fixed central point $\mathbf{u}_0$, which corresponds to the spherical orbit, $\xi = \mathrm{const}$, and around which all KAM curves of quasiperiodic orbits are formed. The position $\mathbf{R}_i = \mathbf{u}_i - \mathbf{u}_0$ of each crossing point $\mathbf{u}_i$ of a phase-space trajectory on the surface of section with respect to $\mathbf{u}_0$ is defined. Finally the angles $\theta_i = \mathrm{angle}(\mathbf{R}_{i+1}, \mathbf{R}_i)$ between two successive positions of $\mathbf{R}_i$ on the surface of section are calculated.

The rotation number is intimately related to the ratio of fundamental frequencies of the orbit itself. On KAM tori the ratio of frequencies is irrational and varies from one curve to the other, so the rotation number changes continuously and monotonically as a function of the distance from the center $\mathbf{u}_0$ of the Poincaré section. Its monotonic evolution is interrupted though, creating a plateau, by the islands of the periodic orbits, where the value of ν_θ is rational and fixed for all these orbits belonging to the same chain of islands. All these orbits are characterized by the same frequency ratio, regardless of the specific KAM curve to which each orbit belongs. Within an island of stability, the ratio of frequencies remains constant, even though the frequencies themselves change from one KAM curve to another.

A. The Poincaré section of the perturbed Euler problem

In order to demonstrate that the perturbed Euler problem is nonintegrable we have constructed a Poincaré section and searched for Birkhoff islands. The physical parameters

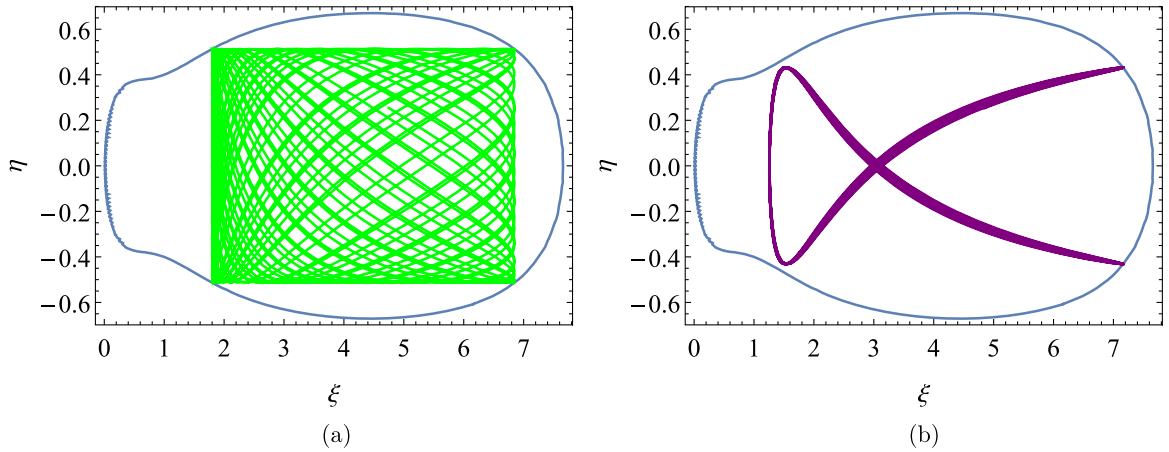

FIG. 1. The CZV (blue boundary) of orbits in a perturbed Euler field with $M_0 = 1$, $a = 0.7$, $\varepsilon = 10^{-2}$. The orbits are characterized by orbital parameters $E = -0.156393$, $L_z = 1.32878$. The left panel, (a), corresponds to an orbit with $\xi(0) = 1.800$ (which leads to a KAM torus in phase space), while the right panel, (b), corresponds to a fine-tuned orbit with $\xi(0) = 1.257$ (which leads to a resonant KAM curve enclosed in a Birkhoff island on the Poincaré section). Both orbits are evolved for the same total time: $T = 500$.

M_0, a, as well as the orbital parameters E, L_z of the perturbed system with $\epsilon = 10^{-2}$ were initially chosen so that there are bound orbits. For such a fixed set of parameters, we evolved numerically a set of orbits with different initial conditions $[\xi(0), \dot{\xi}(0) = 0, \eta(0) = 0$, while the initial velocity $\dot{\eta}(0)$ was calculated directly by Eqs. (15) and (16) apart from its sign, which was chosen to be positive]; see Figs. 1(a) and 1(b). Then we formed the Poincaré section of all these orbits (see Fig. 2) and measured the rotation number of each one. Most of them formed KAM curves on the Poincaré section.

By choosing the particular initial condition $\xi(0)$ that had led to three single fixed points on the Poincaré section in the unperturbed problem corresponding to the resonance of 2:3, and assuming the same parameters M_0, a, E, L_z, we managed to locate the chain of Birkhoff islands of the corresponding nonintegrable system. Fiddling around this initial condition we found a whole set of resonant orbits, belonging to the same chain of Birkhoff islands. Of course all Birkhoff islands are symmetric on the corresponding Poincaré surface of section. Any asymmetries like those found in [34] cannot be reproduced by a Newtonian gravitational field, like the perturbed Euler field, since it cannot lead to noncircular relativistic effects.

We have also drawn the rotation curve (Fig. 3) of all orbits evolved. The strictly monotonic function $\nu_\theta(\xi(0))$ is

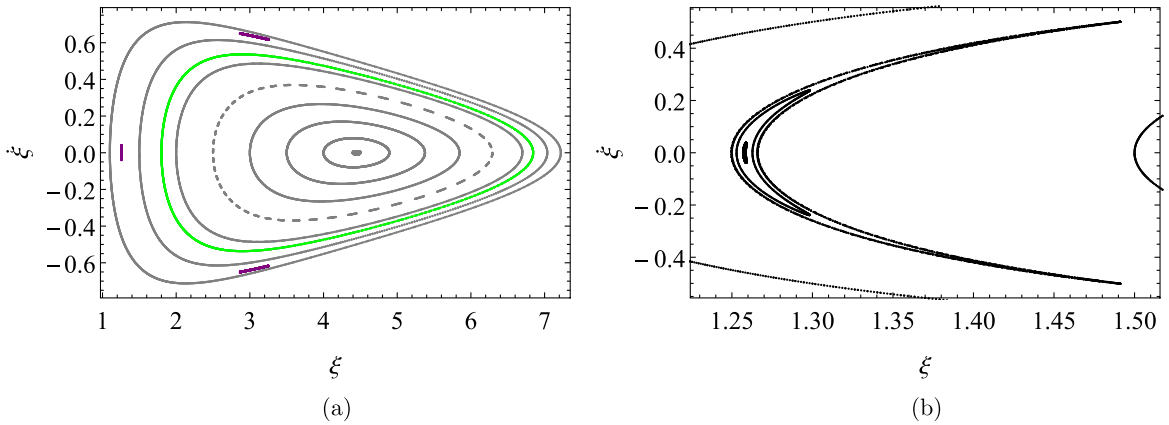

FIG. 2. On the left panel, (a), the Poincaré sections of a number of orbits, all characterized by $E = -0.156393$, and $L_z = 1.32878$ (the same as for the previous Fig. 1), are drawn. Each orbit is evolved starting from a different initial condition $\xi(0)$. Most of the orbits lead to KAM curves [among them is the green KAM curve of the orbit shown in Fig. 1(a)]. Even the apparently dashed curve is a normal KAM curve that needs longer evolution time to fill the whole invariant curve. Also shown is the (purple) chain of Birkhoff islands that correspond to the orbit of Fig. 1(b) with resonance $\Omega_\xi : \Omega_\eta = 2:3$. On the right panel, (b), a detail of the Poincaré section around the purple leftmost island of (a) is drawn. A few other Poincaré sections are shown, all corresponding to the same Birkhoff island of resonance 2:3.

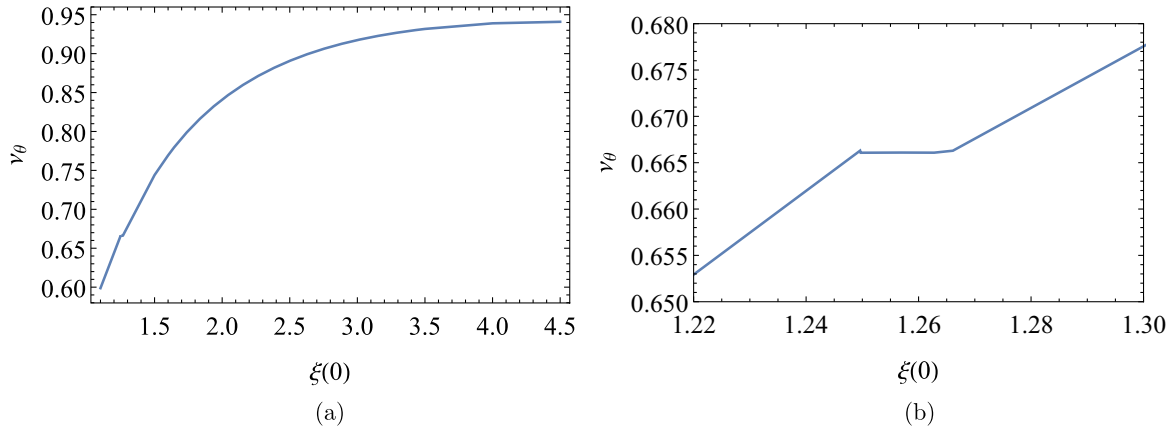

FIG. 3. On the left plot, (a), the rotation number ν_θ as a function of $\xi(0)$ is drawn for orbits with the same physical parameters as the ones presented in the two previous Figures. The horizontal axis spans almost the whole range of allowed $\xi(0)$'s up to the fixed central point u_0 of the Poincaré section of Fig. 2(a). Apart of the anticipated monotonic character of $\nu_\theta(\xi(0))$, it is clear that around $\xi(0) = 1.25$ there is a narrow plateau corresponding to the particular resonance of 2:3. A detail of this plateau is shown on the right panel, (b). The minuscule "glitch" on the left side of the plateau is an indication that the Birkhoff island is surrounded by a very narrow chaotic strip.

interrupted by a narrow plateau, corresponding to all orbits at resonance 2:3; see Fig. 3(b).

The width of the Birkhoff islands is intimately related to the magnitude of the perturbation ϵ. More specifically, for sufficiently small perturbation parameter, the width should scale as $\sqrt{\epsilon}$ (see Refs. [35,36]). We have confirmed this theoretical relation by measuring the width of the leftmost island of resonance 2:3 along the ξ-axis, for a few values of ϵ in the range 10^{-5} to 10^{-2}, see Fig. 4.

Of course a Newtonian gravitational field, like the Euler or the perturbed Euler field, cannot lead to frame dragging or noncircular effects [34].

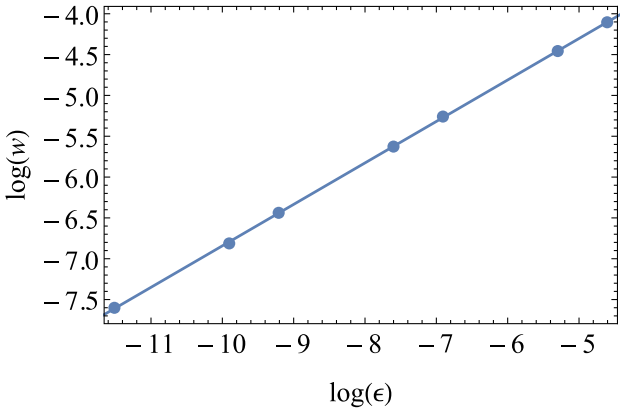

FIG. 4. The width w of the leftmost Birkhoff island of resonance 2:3 [shown in Fig. 2(b) for $\epsilon = 10^{-2}$] has been computed for a few cases (shown as points) of the perturbative parameter $\epsilon = m/M_0$. All points represent orbits with the same orbital parameters E, L_z as in Fig. 1. The best-fit straight line is the $\log(w) = -1.7641 + 0.507812\log(\epsilon)$ which is in accordance with the expected theoretical slope of $1/2$ (see Ref. [35]).

V. INSPIRALS

In the previous section we studied the evolution of orbits in the perturbed Euler gravitational field alone, that is without any additional external force. This can be regarded as the analog of the relativistic geodesic orbits in a specifically perturbed Kerr metric, like the Manko-Novikov metric [17]. The orbit of a compact object in a realistic EMRI though is not exactly geodesic, due to radiation reaction self-force. As long as the ratio of masses of the binary is sufficiently small, the orbits could be considered almost geodesics, but with adiabatically varying orbital parameters. This is true not only for EMRIs with a Kerr black hole as the central object, but with a non-Kerr supermassive central object as well.

In order to probe into the effect of resonance crossing due to an unknown self-force in a perturbed Kerr metric, we have used instead the perturbed Euler problem, endowed with an artificial dissipative self-force, as a trustworthy toy model. Usually, the study of such crossings in various perturbed Kerr background spacetimes is carried out by inducing the average value of energy and z-angular momentum losses to the corresponding geodesic equations of motion [16,18,19]. Although this method leads in general to crude, though sufficiently accurate, adiabatic evolution of orbits, when the orbit passes through a resonance, this approximation becomes unreliable. The evolution of the orbit through a resonance under the instantaneous self-force itself, could be quite different then.

We have studied the evolution of orbits in the perturbed Euler field through a resonance, following two different schemes: (i) By numerically integrating the second-order Euler-Lagrange equations of a test body under the specific Newtonian gravitational force, with a given external dissipative force, and (ii) by numerically integrating a new version of the equations of motion of the Newtonian field

alone, suitably parametrized by the usual integrals of motion, E, L_z, and imposing a prescribed time dependence in E, L_z, caused by the very same dissipative force. In Sec. VI we will further elaborate on the new set of equations employed by the second scheme.

The evolution of the first scheme describes, up to numerical errors, the right evolution of the orbit, while the second scheme gives an approximate evolution of the orbit. When the orbit is not at resonance, the two different schemes are expected to lead to approximately equivalent adiabatic evolutions at the limit of zero self-force. Since the corresponding torus in phase space is then densely covered, one should not anticipate any difference in the estimation of average losses, if these are measured either along an adiabatic geodesic orbit (as in the second scheme), or along the actual orbit under a tiny self-force.

In order to check how generic are our results with respect to the differences arising by applying the two schemes described above, we have used two different dissipative forces, as analogs of the relativistic self-force. The general formula assumed for both external forces is

$$\mathbf{F}_{\rm ext} = -\delta\mu f(\xi,\eta)\mathbf{v}, \tag{24}$$

where μ is the mass of the test particle, $\mathbf{v}$ is its vector velocity, $\delta \ll 1$ measures the magnitude of the self-force, and the function $f(\xi,\eta)$ determines how the strength of this force depends on the actual position of the particle. The two cases investigated were

$$f_1(\xi,\eta) = 1, \tag{25}$$

$$f_2(\xi,\eta) = \frac{\sqrt{1-\eta^2}}{\xi}. \tag{26}$$

The first function f_1 corresponds to the usual atmospheric drag force, while the second one, f_2 has been constructed so as to lead to a loss of energy and angular momentum, while its strength is enhanced at lower ξ values, where the field is stronger, and depends on the η-coordinate in a simple but physical, reflection-symmetric way.

The components of velocity $\mathbf{v}$ in oblate spheroidal coordinates are (see Appendix A of [20]),

$$v_\xi = a\dot{\xi}\sqrt{\frac{\xi^2+\eta^2}{\xi^2+1}}, \tag{27}$$

$$v_\eta = a\dot{\eta}\sqrt{\frac{\xi^2+\eta^2}{1-\eta^2}}, \tag{28}$$

$$v_\phi = a\dot{\phi}\sqrt{(1-\eta^2)(\xi^2+1)}. \tag{29}$$

The instantaneous energy and z-angular momentum losses per unit mass are given from

$$\left(\frac{dE}{dt}\right)_i = \mathbf{v}\cdot\mathbf{a}_{\rm ext} = -\delta a^2 f_i(\xi,\eta)\left[(\xi^2+\eta^2)\left(\frac{\dot{\xi}^2}{1+\xi^2}+\frac{\dot{\eta}^2}{1-\eta^2}\right)+(1+\xi^2)(1-\eta^2)\dot{\phi}^2\right], \tag{30}$$

$$\left(\frac{dL_z}{dt}\right)_i = \hat{\mathbf{z}}\cdot(\mathbf{v}\times\mathbf{a}_{\rm ext}) = -\delta a^2 f_i(\xi,\eta)(1+\xi^2)(1-\eta^2)\dot{\phi}, \tag{31}$$

where $\mathbf{a}_{\rm ext} = \mathbf{F}_{\rm ext}/\mu$ and i-index denotes the type of self-force used; see Eqs. (25) and (26). The average loss of either E or L_z at each orbital point is computed by

$$\left\langle\frac{dK}{dt}\right\rangle = \lim_{T\to\infty}\frac{1}{T}\int_0^T\frac{dK}{dt}dt, \tag{32}$$

where K stands for E or L_z, and the integrant is computed along a geodesic orbit; i.e., an orbit on which no external force is applied. Along this orbit E and L_z are retained. The integration time T need to be infinite so that the geodesic orbit has fully covered the whole available phase space for that orbit. Practically, we have integrated this ratio for such a long time that the ratio converges to a finite value. Of course T should be much longer than the scale of ξ and η oscillations.

VI. ORBITAL EVOLUTION FROM AVERAGED ENERGY AND MOMENTUM LOSSES

In contrast to the Newtonian evolution of an orbit under a given instantaneous dissipative self-force, which is straightforward in the case of an orbit in pure or perturbed Euler potential, the evolution due to the corresponding average losses of energy and z-angular momentum is more complicated. The situation is exactly the opposite in the evolution of an orbit in a perturbed Kerr metric. In this case the self-force itself is not known; actually a complete analytic form is not known for a generic orbit, even in pure Kerr. However, one could easily evolve a geodesic orbit, assuming the energy and the z-angular momentum are given in analytic forms through a hybrid model [18] for orbits in Kerr, suitably adjusted to accommodate for the non-Kerr mass-quadrupole moment of the specific metric [37].

In order to evolve an orbit in a perturbed Euler potential, with a given average loss of energy and z-angular momentum, we cannot rely on Hamiltonian formalism, since there

is no straightforward way to turn a Hamiltonian problem into a dissipative one, that its equations of motion lead to a given time-dependence of the integrals of motion of its nondissipative counterpart. We have overcome this issue by transforming the equations of motion into a Hamiltonian-like form (that is to first-order differential equations), but suitably parametrized by quantities that are equivalent to the integrals of motion when the self-force is absent.

The new set of equations of motion describing the orbit on the polar plane (the azimuthal angle ϕ can be straightforwardly integrated once the angular momentum is given) are differential equations for ξ, η and an additional angle θ defined as

$$\frac{\dot{\xi}}{\sqrt{1+\xi^2}} = A\sin\theta, \tag{33}$$

$$\frac{\dot{\eta}}{\sqrt{1-\eta^2}} = A\cos\theta, \tag{34}$$

with A being the positive-definite kinetic energy along the polar plane

$$A = \frac{\dot{\xi}^2}{\xi^2+1} + \frac{\dot{\eta}^2}{1-\eta^2}. \tag{35}$$

The angle θ is a well defined quantity, related to the ratio of $\dot{\xi}$ and $\dot{\eta}$ terms in A, as long as A is nonvanishing.

The new set of the equations of motion for ξ, η, θ (assuming the mass of the test particle is unity) then reads

$$\dot{\xi} = A\sqrt{1+\xi^2}\sin\theta, \tag{36}$$

$$\dot{\eta} = A\sqrt{1-\eta^2}\cos\theta, \tag{37}$$

$$\dot{\theta} = -A\sin\theta\cos\theta S_1 + \frac{A}{\xi^2+\eta^2}\left(S_2S_3 - 2\sin\theta\cos\theta S_4 + \frac{1}{A^2}\left[\frac{L_z^2 S_5}{a^4} - \frac{GM_0}{a^3}((1-\epsilon)S_6 + \epsilon S_7)\right]\right), \tag{38}$$

where the S_i's are functions of ξ, η, θ:

$$S_1 = \frac{\eta\sqrt{1+\xi^2}\cos\theta + \xi\sqrt{1-\eta^2}\sin\theta}{\sqrt{(1+\xi^2)(1-\eta^2)}}, \tag{39}$$

$$S_2 = -(1-\eta^2)\sin^2\theta + (1+\xi^2)\cos^2\theta, \tag{40}$$

$$S_3 = \frac{\xi\cos\theta}{\sqrt{1+\xi^2}} + \frac{\eta\sin\theta}{\sqrt{1-\eta^2}}, \tag{41}$$

$$S_4 = \eta\sqrt{1-\eta^2}\cos\theta - \xi\sqrt{1+\xi^2}\sin\theta, \tag{42}$$

$$S_5 = \frac{\xi\sqrt{1-\eta^2}\cos\theta + \eta\sqrt{1+\xi^2}\sin\theta}{((1-\eta^2)(1+\xi^2))^{3/2}}, \tag{43}$$

$$S_6 = \frac{\sqrt{1+\xi^2}(\xi^2-\eta^2)\cos\theta - 2\xi\eta\sqrt{1-\eta^2}\sin\theta}{(\xi^2+\eta^2)^2}, \tag{44}$$

$$S_7 = \frac{\xi\sqrt{1+\xi^2}\cos\theta + \eta\sqrt{1-\eta^2}\sin\theta}{(1+\xi^2-\eta^2)^{3/2}}. \tag{45}$$

The A term in the set of equations above is simply a function of the total energy E and z-angular momentum L_z, as well as of the coordinates ξ, η, through

$$A = \sqrt{\frac{2}{a^2(\xi^2+\eta^2)}\left[E - \frac{L_z^2}{2a^2(1+\xi^2)(1-\eta^2)} - V(\xi,\eta)\right]}. \tag{46}$$

Equation (38) for θ has been derived by computing the time derivative of the ratio between the first two velocities [(36), (37)] in order to eliminate A, and then by introducing the expressions for $\ddot{\xi}$ and $\ddot{\eta}$ from the Euler-Lagrange equations of the perturbed Euler field without any induced self-force, which are given in the Appendix.

Now Eqs. (36)–(38) form a set of three first-order differential equations that describe the evolution of the system under the constrain of a constant energy and z-angular momentum. As long as the A term is nonvanishing, the evolution is equivalent to that of Hamilton's equations. However, if the A term goes to zero, the set of the above equations becomes indeterminate and one cannot use them to evolve the system. The vanishing of the A term though corresponds to a very special set of initial conditions; when both $\dot{\xi}$ and $\dot{\eta}$ get simultaneously zero along the evolution. This situation arises when the orbit touches the zero-velocity curve which could be obtained by extremely fine tuning of initial conditions, corresponding to zero measure. Therefore we do not expect this singular case to arise when arbitrary initial conditions are evolved for a finite time. An orbit, though, might actually come very close to the CZV. However, one should not be worried about that, as long as the A does not drop below a given threshold; the numerical errors in the

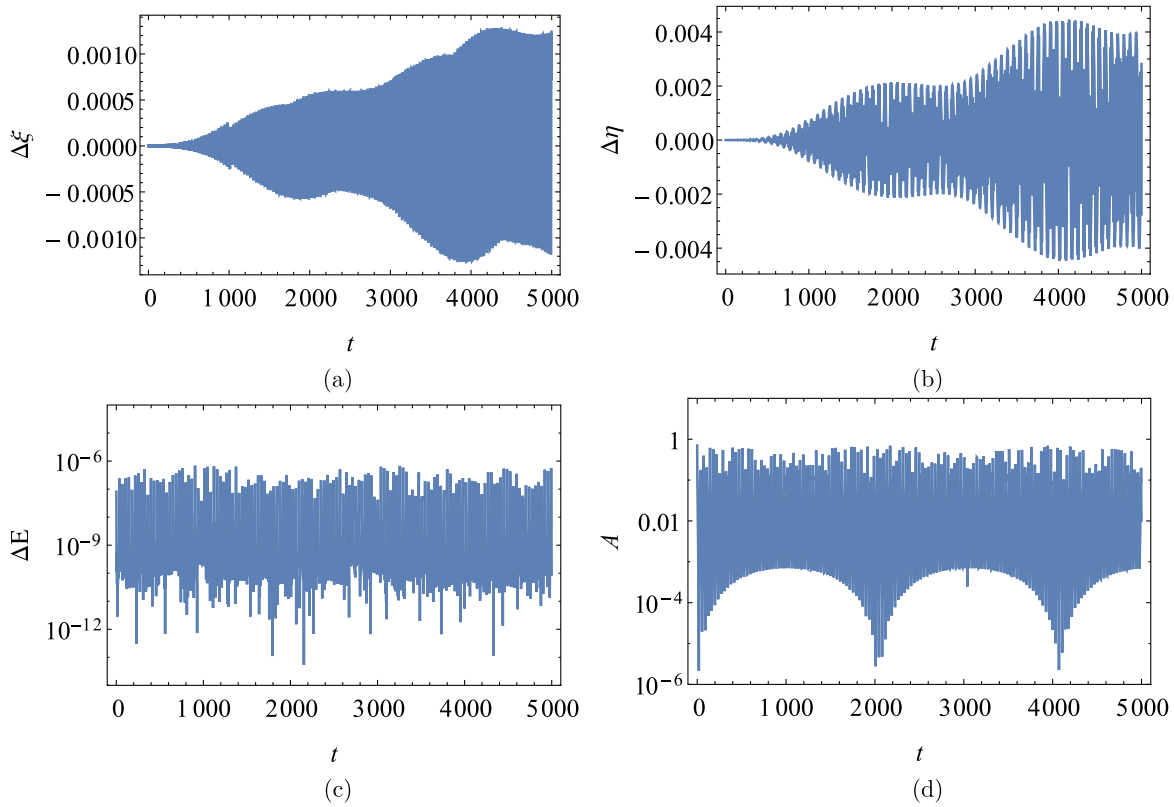

FIG. 5. The plots demonstrate the typical level of numerical accuracy in orbital evolution under the two integration schemes. In the upper two plots, (a) and (b), we have drawn the deviation of $\xi(t)$ and $\eta(t)$, respectively, between the two integration schemes. In the bottom-left plot, (c), the evolution of the deviation of the energy E, under the second scheme is presented. Finally, in the bottom-right plot, (d), we have drawn the evolution of the parameter A used in the second scheme (described in Sec. VI). The orbital evolution in all these diagrams refers to a quasi-periodic orbit with the same physical and orbital parameters used in Fig. 1, and with initial conditions $\xi(0) = 1.270$, $\eta(0) = \dot{\xi}(0) = 0$.

evolution of the set of first-order differential equations given above are then restricted.

The advantage of the new set of equations is that they give us the opportunity to evolve the orbit with a predetermined time-varying law for E and L_z. This is what we will exploit to compare the evolution of an orbit under a self-force with its evolution under the corresponding constant rate of change of energy and z-angular momentum.

A. Accuracy tests

We have used *Mathematica* in order to integrate numerically either scheme of orbital evolution. In order to test the numerical accuracy of integration we first run the equations of motion (A2) for a few initial conditions without imposing any self-force. We run also the system of equations (36), (37), and (38) for the same initial conditions, with a constant value of the parameters E, L_z, equal to the energy and z-angular momentum corresponding to the initial conditions. Then we measure the orbital deviations between the two schemes. What we found (see Fig. 5) is that there is some secular increase in the deviations of $\xi(t)$ and $\eta(t)$, caused by numerical errors, which are of order $\mathcal{O}(10^{-3})$ for a total time of 5000. As a comparison, the actual oscillations of ξ and η are of order ~ 7 and $\mathcal{O}(10^{-1})$, respectively, with oscillation periods of order ~ 30 and ~ 70, respectively. Moreover, we have tested the invariance of the conserved quantity E, under the second scheme of integration. The deviations of E did not exceed 10^{-6} for the same total time of evolution. Also, we have monitored the evolution of the parameter A, along the integration, to ensure that the new set of equations does not lead to erroneous orbital evolution due to indeterminacy of the equations themselves. In all cases we have verified that the value of A did not drop below 10^{-7}, which is quite safe for the accuracy of *Mathematica's* numerical solver.

VII. COMPARISONS BETWEEN THE TWO SCHEMES AND CONCLUSIONS

The gravitational waves emitted by an EMRI, the central source of which is not a pure Kerr black hole, are expected to demonstrate, due to non-integrability, a peculiar behavior when a resonance is met [16,19]. The ratio of the fundamental frequencies encoded in the signal will remain constant, while the system crosses a Birkhoff chain of

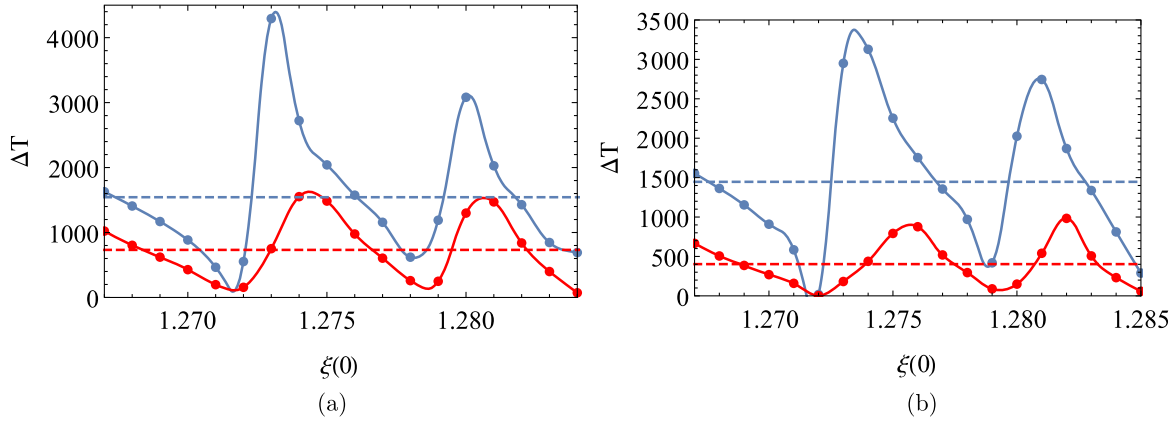

FIG. 6. These plots show how the crossing time for a Birkhoff island depends on the initial position of an orbit when (i) the orbit evolves under an instantaneous self-force (blue curves), or (ii) the orbit evolves by imposing a specific average loss of E, and L_z (red curves), computed when the orbit enters the resonance, which corresponds to the particular self-force. The left panel, (a), is for the case of air-drag-type force (f_1) with $\delta = 10^{-6}$, while the right panel, (b), is for the more complicate type of self-force (f_2) with $\delta = 5 \times 10^{-6}$. The horizontal dashed lines, in both plots, represent the averages of all crossing-times in each case. The ups and downs of these plots are due to the fact that, depending on the entrance point, the orbital evolution through an island could be either very short or quite long.

islands. The duration of this crossing is essential to discern such a nonintegrable, with regard to the corresponding equations of motion, background spacetime. All cases of non-integrable EMRIs studied up to now are evolved by imposing a specific rate of loss in E and L_z directly in the equations of motion, either inside or outside a resonance. The evolution under the actual self-force is not guaranteed to lead to the same duration of resonance crossing, though.

In order to study the differences in crossing time of a given resonance arising from the evolution of the two different schemes described in Sec. V, we constructed a sequence of initial conditions quite close to the concave side of the leftmost Birkhoff island of the 2:3 resonance [see Fig. 2(b)], and evolved them directly with the instantaneous self-force scheme up to the point where the particular resonance is hit.

Subsequently, we followed two different ways to further evolve the orbit: (i) using the same scheme, up to the point where the orbit exits the corresponding Birkhoff island; and (ii) computing the average losses of E and L_z at the specific phase-space coordinates when the orbit first enters the Birkhoff island and imposing these losses in Eqs. (36)–(38) of the second scheme until the orbit, again, exits the island. The E and L_z parameters introduced in these equations, through A and L_z, were assumed to vary linearly with time, with time derivatives given by the losses mentioned above.

During the orbital inspiral, we periodically examined if the orbit is at resonance. This involved pausing the evolution using either integration scheme, then progressing the system along a geodesic, assuming there were no self-force, and plotting its Poincaré section. The orbit was considered to be at resonance, if a chain of Birkhoff islands forms on the Poincaré section.

For each unique evolution, we recorded the total time that the orbit spends within the island. The obtained results are presented in Fig. 6, illustrating the outcomes for the two types [(25), (26)] of self-force employed in our analysis. Depending on the entrance point, the evolution of an orbit inside a chain of Birkhoff islands varies significantly; the orbit may get trapped at resonance for quite a long time, or pass the resonance in a very short period. This explains the recurrent ups and downs shown in the diagram, for both integration schemes in either type of self-force assumed. This feature is reminiscent of the time intervals presented in Fig. 11 of [16], where the crossing time of the resonance 2:3 for the relativistic nonintegrable case of Manko-Novikov was studied.

It is clear that the scheme based on average losses leads to systematic and significant lower values of crossing times, compared to the crossing times under the instantaneous action of the self-force itself. The crossing time due to the actual evolution of the orbit is on average 2 to 3.5 times larger than what one would get by imposing the fixed values for the losses of E and L_z, computed at the entrance point, during the whole evolution.

Actually, several distinct orbital evolutions were conducted using different types of self-force, different magnitudes of δ and ϵ, and different orbital parameters E, L_z. The crossing time, when the self-force was employed to evolve the orbit, was boosted in all cases by a factor similar, if not greater, to the case analyzed in Fig. 6.

The Newtonian analog used in this paper is indicative of the differences arising in the evolution of an orbit through a resonance of a slightly nonintegrable system under the two different integration schemes. Moreover the similarity of the Kerr metric with the Euler problem suggests that these results represent what one would expect in a generically perturbed Kerr system. Therefore, all estimations of the duration of the plateau effect in a slightly perturbed relativistic integrable system presented in the literature up to now [16,19], might be suppressed, compared to the

actual duration of this effect in realistic EMRIs. For example for an EMRI with ratio of masses 10^{-6} and central mass $M = 10^6 M_\odot$, a plateau which was numerically estimated to last for ~5 days, based on average losses, could actually last for more than ~10 days.

ACKNOWLEDGMENTS

Research was supported by the Programme for the promotion of the exchange and scientific cooperation between Greece and Germany IKYDA 2022. Also, A. E. would like to thank K. Kokkotas for his hospitality at Eberhard Karls Universität Tübingen, during which a large part of the computations were performed.

APPENDIX: EQUATIONS OF MOTION

The Lagrangian L per unit mass of the perturbed Euler field is given by

$$L = p_\mu \dot{q}_\mu - H, \tag{A1}$$

where H is the Hamiltonian of Eq. (13), p_μ are the conjugate momenta given in Eqs. (4)–(6) and $\dot{q}_\mu = (\dot{\xi}, \dot{\eta}, \dot{\phi})$. The equations of motion, that were solved numerically under the first scheme, are given by the Euler-Lagrange equations,

$$\begin{aligned}
\ddot{\xi} &= \frac{\xi}{\xi^2+\eta^2}\left(-\dot{\xi}^2\frac{1-\eta^2}{\xi^2+1} + \dot{\eta}^2\frac{\xi^2+1}{1-\eta^2}\right) - \frac{2\eta\dot{\eta}\,\dot{\xi}}{\xi^2+\eta^2} + \frac{\xi(\xi^2+1)(1-\eta^2)}{\xi^2+\eta^2}\dot{\phi}^2 \\
&\quad - \frac{G(M_0-m)}{a^3}\frac{(\xi^2+1)(\xi^2-\eta^2)}{(\xi^2+\eta^2)^3} - \frac{Gm}{a^3}\frac{\xi(\xi^2+1)}{(\xi^2+\eta^2)(1+\xi^2-\eta^2)^{3/2}}, \\
\ddot{\eta} &= -\frac{\eta}{\xi^2+\eta^2}\left(-\dot{\xi}^2\frac{1-\eta^2}{\xi^2+1} + \dot{\eta}^2\frac{\xi^2+1}{1-\eta^2}\right) - \frac{2\xi\dot{\eta}\,\dot{\xi}}{\xi^2+\eta^2} - \frac{\eta(\xi^2+1)(1-\eta^2)}{\xi^2+\eta^2}\dot{\phi}^2 \\
&\quad - \frac{G(M_0-m)}{a^3}\frac{2\xi\eta(1-\eta^2)}{(\xi^2+\eta^2)^3} - \frac{Gm}{a^3}\frac{\eta(1-\eta^2)}{(\xi^2+\eta^2)(1+\xi^2-\eta^2)^{3/2}}, \\
\ddot{\phi} &= \left(-\frac{2\xi\dot{\xi}}{\xi^2+1} + \frac{2\eta\dot{\eta}}{1-\eta^2}\right)\dot{\phi}.
\end{aligned} \tag{A2}$$

[1] P. Amaro-Seoane *et al.*, Laser interferometer space antenna, arXiv:1702.00786.
[2] F. D. Ryan, Gravitational waves from the inspiral of a compact object into a massive, axisymmetric body with arbitrary multipole moments, Phys. Rev. D **52**, 5707 (1995).
[3] R. P. Kerr, Gravitational Field of a Spinning Mass as an Example of Algebraically Special Metrics, Phys. Rev. Lett. **11**, 237 (1963).
[4] R. Geroch, Multipole moments. II. Curved space, J. Math. Phys. (N.Y.) **11**, 2580 (1970).
[5] R. O. Hansen, Multipole moments of stationary space-times, J. Math. Phys. (N.Y.) **15**, 46 (1974).
[6] B. Carter, Hamilton-Jacobi and Schrodinger separable solutions of Einstein's equations, Commun. Math. Phys. **10**, 280 (1968).
[7] W. Schmidt, Celestial mechanics in Kerr spacetime, Classical Quantum Gravity **19**, 2743 (2002).
[8] Y. Mino, M. Sasaki, and T. Tanaka, Gravitational radiation reaction to a particle motion, Phys. Rev. D **55**, 3457 (1997).
[9] T. C. Quinn and R. M. Wald, Axiomatic approach to electromagnetic and gravitational radiation reaction of particles in curved spacetime, Phys. Rev. D **56**, 3381 (1997).
[10] E. Poisson, A. Pound, and I. Vega, The motion of point particles in curved spacetime, Living Rev. Relativity **14**, 7 (2011).
[11] L. Barack and A. Pound, Self-force and radiation reaction in general relativity, Rep. Prog. Phys. **82**, 016904 (2019).
[12] M. van de Meent, Gravitational self-force on generic bound geodesics in Kerr spacetime, Phys. Rev. D **97**, 104033 (2018).
[13] É. É. Flanagan and T. Hinderer, Transient Resonances in the Inspirals of Point Particles into Black Holes, Phys. Rev. Lett. **109**, 071102 (2012).
[14] H. Poincaré, Sur un théorème de géométrie, Rend. Circ. Mat. Palermo **33**, 375 (1912).
[15] G. D. Birkhoff, Proof of Poincaré's geometric theorem, Trans. Am. Math. Soc. **14**, 14 (1913).
[16] G. Lukes-Gerakopoulos, T. A. Apostolatos, and G. Contopoulos, Observable signature of a background deviating from the Kerr metric, Phys. Rev. D **81**, 124005 (2010).
[17] V. S. Manko and I. D. Novikov, Generalizations of the Kerr and Kerr-Newman metrics possessing an arbitrary set of mass-multipole moments, Classical Quantum Gravity **9**, 2477 (1992).

[18] J. R. Gair and K. Glampedakis, Improved approximate inspirals of test bodies into Kerr black holes, Phys. Rev. D **73**, 064037 (2006).
[19] K. Destounis and K. D. Kokkotas, Gravitational-wave glitches: Resonant islands and frequency jumps in nonintegrable extreme-mass-ratio inspirals, Phys. Rev. D **104**, 064023 (2021).
[20] A. Eleni and T. A. Apostolatos, Newtonian analogue of a Kerr black hole, Phys. Rev. D **101**, 044056 (2020).
[21] L. Euler, De Motu Corporis ad Duo Centra Virium Fixa Attracti, Novi Commet. Acad. Scient. Imperial Petropolit. **10**, 207 (1766).
[22] H. Keres, Physical interpretation of solutions of the Einstein equations, Sov. J. Exp. Theor. Phys. **25**, 504 (1967).
[23] W. Israel, Source of the Kerr metric, Phys. Rev. D **2**, 641 (1970).
[24] C. M. Will, Carter-like constants of the motion in Newtonian gravity and electrodynamics, Phys. Rev. D **102**, 061101 (2009).
[25] J. P. Vinti, Improvement of the spheroidal method for artificial satellites, Astron. J. **74**, 25 (1969).
[26] K. Glampedakis and T. A. Apostolatos, The separable analogue of Kerr in Newtonian gravity, Classical Quantum Gravity **30**, 055006 (2013).
[27] L. D. Landau and E. M. Lifshitz, *Mechanics*, 3rd ed. (Butterworth-Heinemann, Oxford, 1976).
[28] I. Bizyaev and I. Mamaev, Bifurcation diagram and a qualitative analysis of particle motion in a Kerr metric, Phys. Rev. D **105**, 063003 (2022).
[29] A. J. Lichtenberg and M. A. Lieberman, *Regular and Chaotic Dynamics* (Springer-Verlag, Berlin, 1992).
[30] N. Kolmogorov, On conservation of conditionally periodic motions for a small change in Hamilton's function, Dokl. Akad. Nauk SSSR **98**, 527 (1954).
[31] V. I. Arnold, Small denominators and the problem of stability of motion in classical and celestial mechanics, Russ. Math. Surv. **18**, 85 (1963).
[32] J. Moser, On invariant curves of area-preserving mappings on an annulus, Nachr. Akad. Wiss. Göttingen Math.-Phys. Kl. **II**, 1 (1962).
[33] G. Contopoulos, *Order and Chaos in Dynamical Astronomy* (Springer Berlin, Heidelberg, 2002).
[34] C.-Y. Chen, H.-W. Chiang, and A. Patel, Resonant orbits of rotating black holes beyond circularity: Discontinuity along parameter shift, Phys. Rev. D **108**, 064016 (2023).
[35] G. Lukes-Gerakopoulos and V. Witzany, Nonlinear effects in EMRI dynamics and their imprints on gravitational waves, in *Handbook of Gravitational Wave Astronomy* (2021), p. 42, 10.1007/978-981-15-4702-7_42-1.
[36] V. Arnold, V. Kozlov, and A. Neishtadt, *Mathematical Aspects of Classical and Celestial Mechanics*, 3rd ed. (Springer International Publishing, New York, 2006), ISBN: 978-3-540-48926-9.
[37] J. R. Gair, C. Li, and I. Mandel, Observable properties of orbits in exact bumpy spacetimes, Phys. Rev. D **77**, 024035 (2008).